東北大学機関リポジトリ
TOUR
Tohoku University Repository

Intensity of the resonance Raman excitation spectra of single-wall carbon nanotubes

Intensity of the resonance Raman excitation spectra of single-wall carbon nanotubes

J. Jiang,[1] R. Saito,[1] A. Grüneis,[2] S. G. Chou,[3] Ge. G. Samsonidze,[4] A. Jorio,[5,6] G. Dresselhaus,[7] and M. S. Dresselhaus[4,5]

[1]*Department of Physics, Tohoku University, Sendai 980-8578, Japan, and CREST, JST, Sendai 980-8578, Japan*

[2]*Institute for Solid State Research, Leibniz Institute for Solid State and Materials Research, 01069 Dresden, Germany*

[3]*Department of Chemistry, Massachusetts Institute of Technology, Cambridge, Massachusetts 02139-4307, USA*

[4]*Department of Electrical Engineering and Computer Science, Massachusetts Institute of Technology,*
Cambridge, Massachusetts 02139-4307, USA

[5]*Department of Physics, Massachusetts Institute of Technology, Cambridge, Massachusetts 02139-4307, USA*

[6]*Departamento de Física, Universidade Federal de Minas Gerais, Belo Horizonte, Minais Gerais 30123-970, Brazil*

[7]*Francis Bitter Magnet Laboratory, Massachusetts Institute of Technology, Cambridge, Massachusetts 02139-4307, USA*

The electron-phonon matrix elements are calculated for the radial breathing mode (RBM) and the G-band A symmetry mode of single-wall carbon nanotubes. The RBM intensity decreases with increasing nanotube diameter and chiral angle. The RBM intensity at van Hove singular k points is larger outside the two-dimensional Brillouin zone around the K point than inside the Brillouin zone. For the G band A symmetry mode, the matrix element shows that all semiconducting nanotubes have nonzero LO mode intensity, and the LO mode generally has a larger intensity than the TO mode, while the ratio of the intensity of the LO mode to that of the TO mode decreases with increasing chiral angle. In particular, zigzag nanotubes have zero intensity for the TO mode, and armchair nanotubes have zero intensity for the LO mode. Using the matrix elements thus obtained, the resonance Raman excitation profiles are calculated for nanotube samples under different broadening factor γ regimes. For semiconducting nanotubes, the excitation profiles for the RBM are consistent with experiments. For metallic nanotubes, a quantum interference effect in the Raman intensity is found for both the RBM and LO modes. For the RBM and LO modes, different kinds of excitation profiles are discussed for nanotube samples in the large and small γ regimes by considering the electron-phonon matrix element and the trigonal warping effect. For nanotube samples in the large γ regime, a shift in the energy of the peak in the RBM intensity relative to the corresponding peak in the joint density of states is found.

PACS number(s): 78.67.Ch, 78.40.−q, 78.30.−j

I. INTRODUCTION

Raman spectroscopy has provided a noninvasive, contactless method of sample characterization, and a method for studying the electronic and vibrational properties of single-wall carbon nanotubes (SWNTs).[1,2] Resonance enhancement in the Raman cross section can be observed when the energy separation E_{ii} for an optical transition is close to the laser excitation energy E_L.[1] As for the first-order Raman processes, the RBM and the G-band mode are known to have strong intensity in the lower (near $100–400$ cm^{-1}) and higher (~ 1600 cm^{-1}) frequency regions, respectively. In the radial breathing mode (RBM) mode, all carbon atoms move coherently in the radial direction. The RBM frequency is proportional to the inverse diameter (d_t^{-1}) of the tube and can be described by an empirical relation.[3,4] Raman spectroscopy for the RBM is therefore often used to determine the diameter or diameter distribution in SWNT samples[5,6] and is further used to assign the chiral index (n,m) of individual SWNTs by considering their resonant transitions.[7–9]

The Raman-active G band consists of A, E_1, and E_2 symmetry modes.[4,10,11] Each symmetry mode splits into a TO mode and a LO mode because of both a zone folding[12,13] and a curvature effect.[14] Experiments have provided strong evidence for the importance of SWNT chirality for the G-band Raman intensity.[15,16]

Theoretically, both an *ab initio*[17] and a symmetry-adapted

nonorthogonal tight-binding model[18] were used to derive the electron-phonon (e-ph) matrix element (M) for the RBM, where the deformation potential was assumed to be equal to the first derivative of the transition energy with respect to the nanotube radius. In a previous paper,[15] the nonresonant bond-polarization theory was applied to calculate the G-band Raman intensity, and the calculated chirality dependence of the G-band intensity was shown to be consistent with the experimental results.[15]

So far we have developed computer programs to calculate the e-ph interaction in graphite and SWNTs based on first-order, time-dependent perturbation theory.[19–21] We have applied these e-ph matrix elements to study the relaxation processes for photoexcited electron-hole pairs in graphite and SWNTs.[19,20] The calculated relaxation time is consistent with experiments.[22–27] In graphite we find far infrared light emission at a certain energy close to the Fermi level.[19] In SWNTs, various kinds of phonon-assisted electron-hole relaxation processes in the photoluminescence excitation spectra are predicted, including a one-phonon process, a hot-electron luminescence process, a Raman process, and these processes can well explain the photoluminescence excitation spectra observed experimentally.[28,29]

In this paper, we further apply the e-ph matrix elements M to a calculation of the first-order Raman intensity as a function of E_L.[30] The chirality dependence of the matrix element at E_{ii} is studied in detail for both the RBM and G-band

modes. For the G band, due to the depolarization effect, the electronic response for light polarization perpendicular to the tube axis is strongly suppressed.[31] Correspondingly, polarized Raman measurements show that the G-band Raman scattering is the strongest in the case where both the incident and scattered light polarizations are parallel to the tube axis.[14] Thus, we here restrict ourselves to consider only the A symmetry, which is expected to have the largest intensity. The dependence of the matrix element on chirality can well explain the dependence of the Raman intensity on chirality observed by experiments.[15,16,32]

The optical transition energies E_{ii} can be obtained by both resonance Raman spectroscopy and photoluminescence.[33,34] In Raman spectroscopy, the E_{ii} energies can be obtained by analyzing the Stokes (S) or anti-Stokes (AS) Raman intensity peak positions or by measuring the anti-Stokes and Stokes Raman spectra on the same isolated SWNT.[35]

For a sodium dodecyl sulfate (SDS) wrapped SWNT sample, the RBM resonance Raman spectroscopy window is about 0.06 eV (Ref. 33) and the two peaks corresponding to the incident and scattered resonance conditions cannot be resolved, because the resonance window, i.e., the broadening factor, γ (≈ 0.06 eV) is too large.[33] By calculating the resonance Raman excitation profiles (RRPs), we find in the present work that for the SDS wrapped samples, the peak positions for the RBM intensity are neither at E_{ii}, nor at $E_{ii}+E_{RBM}$ (where E_{RBM} is the RBM phonon energy), but rather are at $E_{ii}+(E_{RBM}/2)$, which indicates the importance of finding a proper correction factor for the experimental methods in order to get reliable E_{ii} energies from Raman spectroscopy for samples with large γ values.

Experimentally, there are other kinds of SWNT samples, namely, SWNTs on a Si substrate or freely suspended SWNTs, where the broadening factor γ is 10 times smaller than that for the SDS wrapped samples.[36] For such a kind of sample, it is possible to resolve the incident and scattered resonance peaks in the RBM Raman spectra. Thus, we study here the RRPs for samples in both the large and small γ regimes.

In comparison to semiconducting nanotubes, metallic nanotubes have different characteristics in both Raman spectroscopy and photoluminescence. The lack of an energy gap at the Fermi energy induces a quenching of photoluminescence. The presence of free electrons results in an asymmetrically broadened Breit-Wigner-Fano line shape around the TO mode frequency for G-band scattering.[37] More importantly, the trigonal warping effect in metallic nanotubes introduces two peaks in the joint density of states (JDOS) for each E_{ii} transition.[38] However, the RBM Raman spectra for metallic SDS wrapped SWNTs only show one peak corresponding to the lower energy peak in the JDOS.[32,33] We find in the present work that the e-ph matrix elements inside and outside the two-dimensional (2D) Brillouin zone (BZ) around the K point have opposite signs, and thus there is a positive interference effect between these two peaks in the JDOS. The large γ value and the positive interference effect will merge the two peaks into one peak for some of the metallic nanotubes. Also, the node effect for the higher energy peaks will make the corresponding Raman signals become very weak for nanotubes with large chiral angles. Furthermore, the matrix elements have smaller values for the higher energy peaks. These results can help us to understand the disappearance of the upper energy peak signals in the experimental measurements on metallic nanotubes.[32,33]

Motivated by the observations that for metallic nanotubes the energy spacing between the two peaks in the RBM intensity is decreased by the quantum interference effect, we find in this work an approach for correcting the experimental data to obtain reliable E_{ii} energies from measured Raman spectra for metallic tubes.

We should mention that in this paper we will not consider exciton states, which have been recently pointed out to be relevant for describing the optical spectra of small diameter SWNTs.[39] So far all Raman scattering theories that have been proposed are free electron-hole theories, that is, they neglect excitonic effects. Very recent theoretical works show that without exciton states, the calculated RBM Raman intensity in SWNTs can still explain many experimental measurements well,[17,40] indicating that except for the absolute values, the relative Raman intensities may not be so sensitive to excitonic effects, since the optical matrix elements are only weakly dependent on energy.[41] If excitonic corrections are needed, we believe that these corrections will be smaller in nanotubes with a large diameter ($d_t > 1.1$ nm). We do not focus on small diameter tubes, although we will refer to small diameter nanotubes as appropriate throughout the paper. Furthermore, due to their increased screening, we expect excitonic effects to be less important in metallic nanotubes. Actually, the theoretically calculated exciton binding energy for the metallic (3,3) tube is 10 times smaller than that for the (8,0) tube, a semiconducting tube.[39] By not focusing in this paper on small diameter nanotubes, the results obtained here for the quantum interference effect for metallic nanotubes are informative without considering exciton states.

In Sec. II, we show how to calculate the e-ph matrix elements. In Sec. III, we study the chirality dependence of the e-ph matrix elements for first-order Raman processes. In Secs. IV and V, the resonance Raman excitation spectra for the RBM and G band A symmetry mode are calculated, respectively. In Sec. VI, the theoretical results are discussed in connection with possible future experiments. In Sec. VII, a summary is given.

II. ELECTRON-PHONON MATRIX ELEMENT THEORY

A periodic displacement of atoms around the equilibrium sites gives rise to the e-ph interaction which can be treated in first-order time-dependent perturbation theory.[19] Due to the C_N symmetry of a SWNT,[10] we can treat the matrix elements within the graphene unit cell, which has only one (A,B) carbon atom-pair. A normalized e-ph matrix element from the $\mathbf{k}$ to $\mathbf{k}'$ electronic states coupled by the νth phonon is given by[19,20]

$$M_\nu(\mathbf{k},\mathbf{k}') = \tfrac{1}{2}A_\nu(\mathbf{q})D^\nu(\mathbf{k},\mathbf{k}'), \qquad (1)$$

in which the amplitude of the phonon vibration is

TABLE I. The fitting parameters for the $2p_z$ wave function and the atomic potential of carbon (Ref. 21) where $l=1,2,3,4$ denotes a set of Gaussians.

l	1	2	3	4
I_l	0.050	0.413	1.061	1.046
σ_l (atomic units)	2.165	0.907	0.130	0.387
v_l (Hartree)	−2.134	−1.000	−2.000	−0.740
τ_l (atomic units)	0.250	0.040	1.000	2.800

$$A_\nu(\mathbf{q}) = \left[\frac{\hbar}{N_u m_C \omega_\nu(\mathbf{q})} \right]^{1/2} \quad (2)$$

and the matrix element D_ν is given by

$$D_\nu(\mathbf{k},\mathbf{k}') = \sum_{s,s',\sigma=A,B} \sum_{\mathbf{R}'_s,\mathbf{R}_s} C^*_{s'}(\mathbf{k}') C_s(\mathbf{k}) \mathbf{m}_\sigma(\mathbf{R}_{s'},\mathbf{R}_s) \cdot \mathbf{e}^\nu_\sigma(\mathbf{q})$$
$$\times e^{-i\mathbf{k}'\cdot(\mathbf{R}_{s'}-\mathbf{R}_\sigma)} e^{i\mathbf{k}\cdot(\mathbf{R}_s-\mathbf{R}_\sigma)}. \quad (3)$$

Here N_u, m_C, and ω_ν are the number of graphene unit cells in the SWNT, the mass of a carbon atom, and the phonon eigenvalue for the νth phonon, respectively, while C_s and $\mathbf{e}^\nu_\sigma$ are the electron wave function coefficient and phonon eigenvector, respectively. $\mathbf{R}_s$ and $\mathbf{R}_{s'}$ are the two electron centers, and $\mathbf{R}_\sigma$ is the atomic potential center. In Eq. (3), $\mathbf{m}$ is an atomic deformation potential vector

$$\mathbf{m}_\sigma(\mathbf{R}_{s'},\mathbf{R}_s) = \int \phi(\mathbf{r}-\mathbf{R}_{s'}) \nabla v(\mathbf{r}-\mathbf{R}_\sigma) \phi(\mathbf{r}-\mathbf{R}_s) d\mathbf{r}. \quad (4)$$

The deformation potential vector $\mathbf{m}$ is a three center integral, i.e., with a potential center $\mathbf{R}_\sigma$ and two electron centers $\mathbf{R}_{s'}$ and $\mathbf{R}_s$. $|\mathbf{m}_\sigma|$ has a maximum value (≈ 6.4 eV/Å) when the two electron centers are at the same site and the potential center is on a nearest-neighbor site.[20] Since $|\mathbf{m}|$ quickly decreases with increasing distance between an electron center and the potential center, the electron centers are taken up to the fourth nearest-neighbor in our calculations.[20]

To calculate $\mathbf{m}$, we fit the calculated carbon $2p_z$ orbital and the carbon atomic potential to a set of Gaussians. The electron wave function $\phi(\mathbf{r}-\mathbf{R}_s)$ and the atomic potential $v(\mathbf{r}-\mathbf{R}_\sigma)$ can thus be expressed by

$$\phi(\mathbf{r}-\mathbf{R}_s) = [(x-x_s)\cos\varphi_s + (y-y_s)\sin\varphi_s]$$
$$\times \sum_l I_l \exp\left[-\frac{(\mathbf{r}-\mathbf{R}_s)^2}{2\sigma_l^2} \right],$$

$$v(\mathbf{r}-\mathbf{R}_\sigma) = \frac{1}{|\mathbf{r}-\mathbf{R}_\sigma|} \sum_l v_l \exp\left[-\frac{(\mathbf{r}-\mathbf{R}_\sigma)^2}{2\tau_l^2} \right], \quad (5)$$

where φ_s is the angle from the positive x-axis to the atom at site $\mathbf{R}_s$. We find that by using four Gaussians ($l=1,2,3,4$), both the electron wave function and the atomic potential can be fitted very well. The fitting parameters for these functions are listed in Table I.[21] Substituting Eq. (5) into Eq. (4), the three center integrals for $\mathbf{m}$ can be evaluated analytically.

For the RBM and G band modes with A symmetry, the phonon wave vector for these first order Raman processes is selected as $\mathbf{q}=0$ and thus Eq. (3) can be further simplified to yield

$$D_\nu(\mathbf{k},\mathbf{k}) = \sum_{s,s'=A,B} \sum_{\mathbf{R}_{s'},\mathbf{R}_s}^{N_u} C^*_{s'}(\mathbf{k}) C_s(\mathbf{k}) e^{-i\mathbf{k}\cdot(\mathbf{R}_{s'}-\mathbf{R}_s)}$$
$$\times \mathbf{e}^\nu_A \cdot [\mathbf{m}_A(\mathbf{R}_{s'},\mathbf{R}_s) \pm U(\varphi_{BA})\mathbf{m}_B(\mathbf{R}_{s'},\mathbf{R}_s)], \quad (6)$$

where $+$ and $-$ are for the RBM and the G band modes with A symmetry, respectively, $U(\varphi_{BA})$ with $\varphi_{BA}=\varphi_B-\varphi_A$ is a rotation matrix around the nanotube axis from the B atom to the A atom in the 2D graphite unit cell, and the phonon eigenvectors $\mathbf{e}_A$ for the A atom are given by

$$\mathbf{e}^{RBM}_A = \frac{1}{\sqrt{2}}(1,0,0)$$

$$\mathbf{e}^{TO}_A = \frac{1}{\sqrt{2}}(0,1,0)$$

$$\mathbf{e}^{LO}_A = \frac{1}{\sqrt{2}}(0,0,1). \quad (7)$$

III. CHIRALITY DEPENDENCE OF THE ELECTRON-PHONON MATRIX ELEMENT FOR THE RBM AND G BAND A SYMMETRY MODES

A. RBM electron-phonon matrix element

The e-ph matrix element for an electron-hole pair with wave vector $\mathbf{k}$ is expressed by[17]

$$M(\mathbf{k}) = M(\mathbf{k}_c) - M(\mathbf{k}_v), \quad (8)$$

with $M(\mathbf{k}_c)$ and $M(\mathbf{k}_v)$ the matrix elements for the conduction and valence bands at $\mathbf{k}$, respectively. In Fig. 1, we plot smooth curves[42] for the evaluation of the matrix element along equienergy contours of 1.5, 2.0, and 2.5 eV in the 2D BZ of graphite. The real (n,m) SWNTs would appear as discrete points along the continuous lines in Fig. 1. The $\mathbf{k}$ point in the 2D BZ is selected to be the E^S_{22} van Hove singular (vHS) $\mathbf{k}$ point for semiconducting nanotubes with chiral angle θ. Because of the experimentally observed $(2n+m)$ family effect,[32,33,43] we classify semiconducting nanotubes into two kinds, i.e., the mod $(2n+m,3)=1$ type I (SI) and mod$(2n+m,3)=2$ type II (SII) semiconducting nanotubes.[43] From the Kataura plot,[32,33,43,44] it is known that the SWNT diameters d_t corresponding to $E^S_{22}=1.5$, 2.0, and 2.5 eV are in the range of 1.16–1.30, 0.86–1.00, and 0.64–0.80 nm, respectively. Thus, the transition energy dependence directly reflects the SWNT diameter dependence. Figure 1(a) shows that the value of $|M|$ generally decreases with increasing chiral angle. Moreover, M increases with increasing transition energy E^S_{22}, indicating that $|M|$ decreases with
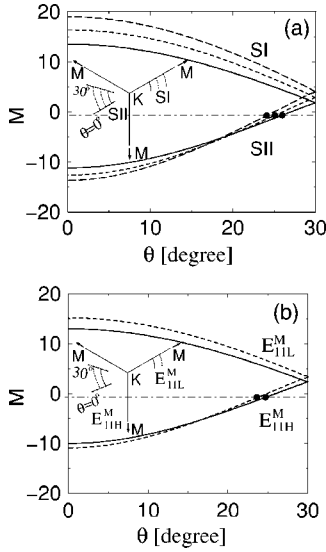
FIG. 1. The chiral angle dependence of the e-ph matrix element M of the RBM for (a) the E_{22}^S transition for semiconducting nanotubes, and (b) the E_{11}^M transition for metallic nanotubes. The matrix element M is in units of $\sqrt{\hbar/(N_u m_C)}$ with N_u and m_C the number of graphene unit cells in the SWNT and the mass of a carbon atom. (a) Upper and lower curves are for SI and SII nanotubes, and solid, dashed, and long-dashed curves are for transition energies 1.5, 2.0, and 2.5 eV, respectively. The inset shows the vHS positions in the 2D BZ. The SI vHSs are outside the 2D BZ of graphite and the SII vHSs are inside the 2D BZ, defined by the symmetry points K and M. (b) Upper and lower curves are for vHSs with lower E_{11L}^M and higher E_{11H}^M energies, and solid and dashed curves are for transition energies 2.0 and 2.5 eV, respectively. The dots in (a) and (b) indicate the node positions for the corresponding transition energies.

increasing d_t. With the same transition energy, i.e., a similar d_t value, and the same chiral angle, SI tubes have a larger $|M|$ than SII tubes. Furthermore, SI tubes have positive M, while SII tubes generally have negative M. Close to $\theta = 30°$, M for SII tubes changes its sign and at $30°$, M becomes the same for both SI and SII tubes with the same transition energy. We should point out that M has nodes for SII tubes in the high chiral angle range, and the nodes move to a smaller chiral angle range with increasing E_{22}^S energy (see black dots in Fig. 1). The node position for SII tubes is approximately given by

$$\theta_N^{\text{SII}} = 30.08 - 2.05 E_{22}^{\text{SII}}, \tag{9}$$

with θ_N and E_{22}^{SII} in units of degrees and electron volts, respectively. Correspondingly, the RBM Raman peaks for SII SWNTs with θ around θ_N should have very weak intensities. This node effect needs to be checked by future careful experimental work, not within the scope of the present paper. The vHSs for the E_{22}^S transition exist outside and inside of the 2D Brillouin zone around the K point for SI and SII tubes, respectively [see the inset of Fig. 1(a)]. The chirality dependence of M shown in Fig. 1(a) for SI and SII tubes is a general result for vHSs outside and inside the 2D BZ for an E_{ii} transition. That is, $|M|$ decreases with increasing d_t and θ, so that $|M|$ has a larger value outside the 2D BZ than inside

the 2D BZ, and generally M has an opposite sign outside and inside the 2D BZ.

For metallic nanotubes, there are two vHSs for each E_{ii}^M giving rise to a splitting into two peaks E_{iiL}^M and E_{iiH}^M in the JDOS, which can be understood by the trigonal warping effect.[38] The vHS **k** points for the lower and higher energy peaks, E_{iiL}^M and E_{iiH}^M, exist outside and inside the 2D BZ, respectively. A plot similar to Fig. 1(a) for the E_{11}^M transition for metallic nanotubes is shown in Fig. 1(b) with upper and lower curves being for the E_{11L}^M and E_{11H}^M peaks, respectively. Figure 1(b) indicates that a metallic nanotube has a larger RBM intensity for E_{11L}^M than for E_{11H}^M. Moreover, M for the E_{11H}^M vHSs has nodes in the high chiral angle range. Regarding chirality, the node position for the E_{11H}^M vHSs is approximately given by

$$\theta_N^M = 30.27 - 2.17 E_{11H}^M. \tag{10}$$

The opposite sign in M shown in Fig. 1(b) for E_{11L}^M and E_{11H}^M vHSs gives rise to an interesting quantum interference effect in the RBM intensity for metallic nanotubes, which will be discussed in detail in this paper. From the Kataura plot of E_{ii} vs d_t,[33,43,44] we know that with a similar transition energy, the diameter corresponding to the E_{11}^M transition for metallic nanotubes is larger than the diameter corresponding to the E_{22}^S transition for semiconducting nanotubes. Correspondingly, for two curves with the same transition energy, the curve in Fig. 1(b) has a smaller $|M|$ value than the curve in Fig. 1(a).

The chirality dependence of M can explain the chirality dependence of the RBM Raman intensity. The experimental measurements show that the RBM intensity for both metallic and semiconducting nanotubes decreases with increasing d_t and θ, and for E_{22}^S transitions, the SI tubes generally have a larger intensity than SII tubes.[32] These experimental results are consistent with the present theoretical predictions for the e-ph matrix element dependence on chirality.

By assuming that the deformation potential for the RBM is equal to the first derivative of the transition energy with respect to the nanotube radius, a recent *ab initio*[17] calculation pointed out that for a particular E_{ii} transition, $|M|$ is proportional to $1/d_t$, and for nanotubes with a similar d_t, $|M|$ is up to one order of magnitude stronger for zigzag tubes than for armchair tubes. Moreover, the matrix elements of zigzag tubes are found to show either a larger or a smaller magnitude with opposite signs.[17] These results are consistent with the present general results for the diameter and chiral angle dependence of $|M|$ and tube type (SI or SII) dependence of M shown in Fig. 1.

B. *G* band *A* symmetry mode electron-phonon matrix element

The matrix elements for the *G* band *A* symmetry (a) LO and (b) TO modes are shown in Fig. 2, which also shows smooth curves for the evaluation of the matrix elements along the equienergy contours of 1.5 and 2.0 eV for E_{22}^S transitions for SI and SII tubes. It is seen that M for the LO mode has a weak diameter and chiral angle dependence relative to $|M|$, while M for the TO mode has a strong chirality dependence. Figure 2(a) also indicates that M has a different
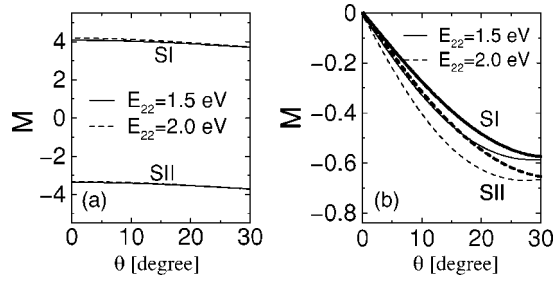
FIG. 2. The chiral angle dependence of the e-ph matrix element of the G band mode with A symmetry: (a) LO mode and (b) TO mode for the E_{22}^S transition. Solid and dashed curves are for the transition energies 1.5 and 2.0 eV, respectively. The matrix element is given in units of $\sqrt{\hbar/(N_u m_C)}$ with N_u the number of graphite unit cells in the SWNT and m_C the mass of a carbon atom. (a) Upper and lower sets of curves are for SI and SII nanotubes, respectively. (b) Thick and thin curves are for SI and SII tubes, respectively.

sign for the LO mode for SI and SII tubes, and furthermore SI tubes have a larger $|M|$ value than SII tubes for a similar d_t and θ except for $\theta=30°$. Moreover, unlike the case of the RBM, $|M|$ for the LO mode remains large, and at $\theta=30°$, M does not become the same, but instead becomes opposite in sign for the SI and SII tubes. For the TO mode, we can see that M has the same sign for SI and SII tubes, and $M=0$ for zigzag tubes, while $|M|$ increases with increasing chiral angle.

Comparing Fig. 2(a) with Fig. 2(b), it is seen that the LO mode always has a larger $|M|$ than the TO mode. We should mention here that the chiral angle dependence of M for SI and SII tubes is a general result for vHSs outside and inside the 2D BZ, respectively, for any E_{ii} transition.

The M dependence of the chirality shown in Fig. 2 can be used to explain the experimental observations for the G band intensity with A symmetry for semiconducting nanotubes.[15,16] Experimental measurements show that the LO mode always has a larger intensity than the TO mode in SWNTs, the ratio between the intensity of the LO and TO modes becoming smaller with increasing chiral angle.[15,16] Furthermore, experiments show that the TO mode has a very small intensity at $\theta\sim0°$.[15,16] These experimental results are consistent with the present predictions from the chirality dependence of M. We should mention that for some special cases, the TO mode can have a similar or even larger intensity than the LO mode for semiconducting nanotubes, which can be explained by the E symmetry phonon modes and the special resonance conditions.[45]

Figure 2 shows M for semiconducting tubes. If we substitute SI and SII in Fig. 2 by E_{11L}^M and E_{11H}^M, respectively, we will get a plot similar to the plot for metallic nanotubes for E_{11}^M energies 1.5 and 2.0 eV. The result that at $\theta=30°$ (armchair nanotubes) M for the LO mode has an opposite sign but the same value for the two vHSs with the same energy outside and inside the 2D BZ is important for explaining the vanishing of the LO mode intensity in armchair (and other $\theta\approx30°$ metallic) tubes. Armchair tubes are special metallic tubes, which have two vHSs with the same energy outside and inside the 2D BZ around the same K point.[10] Their opposite sign and equal M magnitudes causes the LO mode

intensity to be zero in armchair tubes, which agrees with the predictions of group theory.[10]

IV. RBM RESONANCE RAMAN EXCITATION PROFILES

The resonance Raman intensity for first-order modes, such as the RBM and G band, in the Stokes process for a carbon nanotube as a function of laser energy E_L can be calculated by the formula[46]

$$I_S(E_L) = C(n_{\text{ph}}+1)\left(\frac{E_a}{E_e}\right)^2\left(\frac{T}{N_c}\right)\left|\sum_{\mu=0}^{N-1} I^\mu(E_L)\right|^2 \quad (11)$$

where C is a tube-independent constant, E_a ($=E_L$) and E_e are absorption and emission photon energies, respectively, $n_{\text{ph}}=[e^{-\beta E_{\text{ph}}}-1]^{-1}$ is the phonon thermal factor, N_c and T are the number of cutting lines and the one-dimensional (1D) unit vector length of the nanotube, respectively. $I^\mu(E_L)$ is the contribution to the Raman intensity from the μth energy band which is given by

$$I^\mu(E_L) = \int \frac{M^{\text{op}}(\mu,k)MM^{\text{op}}(\mu,k)}{[E_L-E_\mu(k)-i\gamma][E_L-E_\mu(k)-E_{\text{ph}}-i\gamma]}dk \quad (12)$$

For the anti-Stokes process, the phonon number factor ($n_{\text{ph}}+1$) in Eq. (11) should be replaced by n_{ph} and the term $-E_{\text{ph}}$ in the second factor in the denominator of Eq. (12) should be replaced by $+E_{\text{ph}}$. The optical matrix element M^{op} for the electron-photon interaction is calculated by using our previously published formula.[41] The experimentally measured broadening factor γ in Eq. (12) is 0.06 eV for the SDS wrapped SWNT samples,[33] and γ is ten times smaller for isolated SWNTs on a Si substrate.[36] Thus, in our calculations, we take $\gamma=0.06$ and 0.006 eV to model the different experimental regimes for large γ and small γ, respectively. Hereafter, we will mainly discuss the Stokes process. The results for the anti-Stokes process are closely related to those for the Stokes process.

A. Semiconducting nanotubes

In the case of $\gamma=0.06$ eV, the RBM phonon energy is too small to resolve the two resonance conditions for the incident and scattered photons, while in the case of $\gamma=0.006$ eV, it is possible to resolve the two peaks for the two resonance conditions. Therefore, for semiconducting nanotubes, we can see one peak ($\gamma=0.06$ eV) or two peaks ($\gamma=0.006$ eV) in the different γ regimes in the RRP for each E_{ii}^S transition.

1. Large γ case

Figure 3 shows the calculated RBM RRP in the Stokes process for the E_{22}^S transition for (a) an SI type (13,5) tube and (b) an SII type (13,6) tube. The γ value is taken to be 0.06 eV to illustrate the large γ regime. As expected, due to the large γ value, the intensity peak position is neither at E_{22}^S nor at $E_{22}^S+E_{\text{RBM}}$ but rather is at $E_{22}^S+(E_{\text{RBM}}/2)$. Thus, when we try to get the E_{ii} transition energy by analyzing the RBM intensity peak position, we should consider the correction
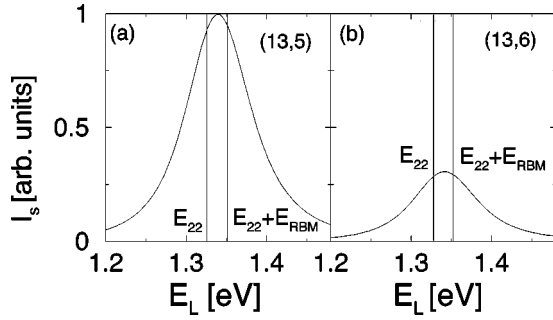
FIG. 3. Calculated Raman intensity in the Stokes process for the RBM vs excitation energy E_L for (a) an SI (13,5) tube and (b) an SII (13,6) tube and using $\gamma = 0.06$ eV.

factor $E_{RBM}/2$. Comparing Fig. 3(a) with Fig. 3(b), it is seen that with a similar d_t and θ, the SI tube has a larger intensity than the SII tube, which follows from the tube type dependence of the matrix element (see Sec. III) and is consistent with experimental observations (Ref. 32).

For the E_{22}^S transition, Eq. (12) indicates that the Raman intensity is dominated by the states at the E_{22}^S band edge, where the resonance condition is satisfied and the JDOS is large. The states for the E_{11}^S band with energies close to E_{22}^S also make a contribution to the intensity since the resonance condition is satisfied. However, these states for the E_{11}^S band are far from the E_{11}^S band edge and the JDOS there is much smaller compared to the JDOS at the E_{22}^S band edge. Thus, these E_{11}^S band states only provide a weak contribution to the observed RBM intensity. The interference effect between the states at the E_{22}^S band edge and the states for the E_{11}^S band in the resonance window will slightly change the RRP shape and will slightly shift the peak position. Thus, the peak position in Fig. 3 cannot be exactly at $E_{22}^S + E_{RBM}/2$. But, the peak position shift from $E_{22}^S + E_{RBM}/2$ should be much smaller than 10 meV since $E_{RBM}/2$ is about 10 meV.

The shape of the RRP in Fig. 3 agrees with experiment.[32,33] In comparison to the JDOS, the asymmetry in the Raman intensity has been decreased due to an interference effect among the states at the band edge. The matrix elements are approximately the same for the states at the band edge. Thus, the matrix element has a negligible effect on the shape of the RBM RRP and the interference effect comes from the denominator of Eq. (12).

By doing experiments with the Stokes and anti-Stokes processes, one can get a so-called accurate experimental value of E_{ii}.[35] For the small γ (~ 0.006 eV) case, the principle of this method has already been discussed.[35] For the large γ case, Fig. 3 indicates that the intensity peak has been shifted by $E_{RBM}/2$ away from E_{ii}. Thus, we would like to know whether or not a correction factor is needed.

Figure 4 shows the calculated RRPs for the RBM for both the Stokes and anti-Stokes processes for the E_{22}^S transition for an SI type (13,5) tube with $\gamma = 0.06$ eV. The normalized anti-Stokes intensity shown in Fig. 4 is obtained by multiplying the measured intensity by $(n_{ph}+1)/n_{ph} \times [(E_L+E_{ph})/(E_L-E_{ph})]^2$. The peaks for the Stokes and anti-Stokes processes in Fig. 4 are at $E_{22}^S + E_{RBM}/2$ and $E_{22}^S - E_{RBM}/2$, respectively. Thus, the E_{22}^S are at the position where the Stokes and nor-

malized anti-Stokes processes have the same intensity. It follows that for the large γ case,[33] we can also get an accurate value of the E_{ii} energy by the same method as is used for the small γ case[35] and no correction factor is needed. The crossing point for the two curves in Fig. 4 is slightly shifted from E_{22}^S due to the interference effect between the states in the E_{11}^S and E_{22}^S bands. The energy shift should be smaller than 10 meV, as we have mentioned earlier.
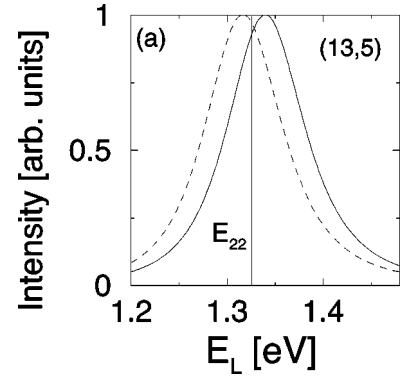

FIG. 4. The RBM Raman intensity vs excitation energy E_L for an SI (13,5) tube. Solid and dashed lines are for Stokes and anti-Stokes processes, respectively, and the plots are for $\gamma = 0.06$ eV (see text for normalization of the anti-Stokes curve).

2. Small γ case

Because of the small phonon energy for the RBM, to clearly see two separated peaks for the incident and scattered resonance in the RBM intensity profile, the broadening factor should be sufficiently small. For a (13,5) or a (13,6) tube with $E_{RBM} \approx 0.023$ eV, the two peaks can be resolved when $\gamma = 0.006$ eV. However, when γ increases to be 0.008 eV, the two peaks can no longer be clearly resolved. For a (10,5) tube with $E_{RBM} \approx 0.028$ eV, the two peaks can already be resolved for $\gamma = 0.008$ eV. The earlier discussion explains why it is difficult to observe two clearly resolved peaks even for SWNTs on a Si substrate for larger d_t SWNTs.[36] The RBM intensities for an (a) SI (13,5) and (b) SII (13,6) with $\gamma = 0.006$ eV are shown in Fig. 5. It is seen that the interference effect between the E_{11}^S and E_{22}^S bands moves the incident and scattered peak positions away from E_{22}^S and $E_{22}^S + E_{ph}$, respectively, by an energy smaller than 10 meV. This means that we can get the E_{ii} energy directly from the RBM intensity peak position and the accuracy for E_{ii} determined in
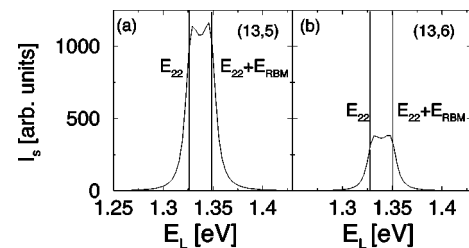

FIG. 5. Raman intensity in the Stokes process for the RBM vs excitation energy E_L for (a) an SI (13,5) tube and (b) an SII (13,6) tube and using $\gamma = 0.006$ eV.

this way is up to 10 meV. Similar to Fig. 3, the results in Fig. 5 also indicate that with a similar d_t and θ, an SI semiconducting tube has a larger intensity than an SII tube.

B. Metallic nanotubes

For metallic nanotubes, the trigonal warping effect in the energy dispersion relation splits each vHS E_{ii}^M peak in the JDOS into two peaks (E_{iiL}^M and E_{iiH}^M, lower and higher energy peaks), depending on the SWNT chirality.[38] Metallic zigzag nanotubes exhibit a maximum splitting, while no splitting is expected for armchair tubes. The splitting energy $\Delta E_{11}^M = E_{11H}^M - E_{11L}^M$ for metallic nanotubes is also inversely proportional to d_t. We calculate the splitting energy by using the extended tight-binding model, which has explicitly included the curvature effect,[18,32,43] for the E_{11}^M transition for all metallic nanotubes with diameters in the range 0.6 nm $< d_t$ < 1.6 nm. We then obtain a functional form $\Delta E_{11}^M(d_t, \theta)$ for the splitting energy that accounts for both the diameter and chiral angle dependence of the splitting energy by fitting the calculated $\Delta E_{11}^M(n,m)$ with

$$\Delta E_{11}^M(d_t, \theta) = \frac{A_1}{d_t} + \frac{B_1}{d_t^2} + \left(\frac{C_1}{d_t} + \frac{D_1}{d_t^2} \right) \cos(3\theta) \quad (13)$$

The parameters that fit to the calculated ΔE_{11}^M are given by $A_1 = 0.01325$ eV nm, $B_1 = -0.03839$ eV nm^2, $C_1 = -0.1839$ eV nm, and $D_1 = 0.7521$ eV nm^2.

For semiconducting nanotubes, the interference effect between the E_{11}^S and E_{22}^S bands is negligible for the RBM, since the JDOS far from the E_{11}^S band edge is small and thus the intensity contribution from those E_{11}^S band states is small. For metallic nanotubes, the situation is quite different. When the energy spacing between the E_{11L}^M and E_{11H}^M peaks in the JDOS is small, the contributions from both peaks are strong and the interference effect between them becomes important. The matrix element M for the RBM has an opposite sign for the E_{11L}^M and E_{11H}^M vHSs [see Fig. 1(b)]. Thus, the sign of M plays an important role in determining the RRP for the RBM in metallic nanotubes due to the quantum interference effect between these two peaks. The quantum interference effect can be a positive or a negative effect, depending on the magnitude of the splitting energy introduced by the trigonal warping effect. We know that, in the laser energy range between E_{11L}^M and E_{11H}^M, the Raman intensity has contributions from both states around E_{11L}^M and around E_{11H}^M. If the contributions from E_{11L}^M and from E_{11H}^M are added together, the intensity is enhanced and this quantum interference effect is a positive effect. Otherwise, if the two contributions are subtracted from each other, the intensity is suppressed and this quantum interference effect is a negative effect. Moreover, Fig. 1 shows that the e-ph matrix element M for the RBM has nodes inside the 2D BZ. This means that the higher energy peaks occurring near the nodes will have a very low intensity. Due to the node effect, the sign of M, the trigonal warping effect and the quantum interference effect, we can have different kinds of RRPs for the E_{11}^M transition for the RBM in metallic tubes.
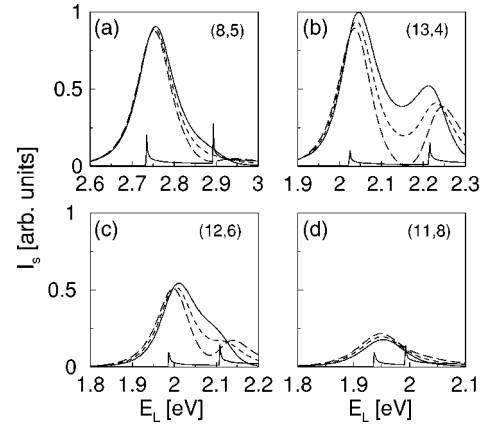

FIG. 6. Illustration of the four kinds of RRPs in the Stokes process for the RBM in metallic nanotubes (a) (8,5), (b) (13,4), (c) (12,6), and (d) (11,8). The profiles calculated by eliminating the interference effect between the contributions from E_{11L}^M and E_{11H}^M and the profiles calculated by taking $|M|$ as the electron-phonon matrix element are also shown by dashed and long-dashed curves. The joint density of states are given to show the vHS peak splitting energy. The broadening factor is $\gamma = 0.06$ eV.

1. Large γ case

In the case of large γ ($=0.06$ eV), we have four kinds of RRPs for the Stokes process for metallic SWNTs and these different RRPs are illustrated in Fig. 6. In order to see clearly the quantum interference effect in the Raman intensity between the states around the E_{11L}^M vHS and the states around the E_{11H}^M vHS, we also calculate the intensity by completely removing the interference between these two contributions. Equation (11) indicates that to obtain the correct total intensity, we should first calculate the two contributions I^{μ_L} and I^{μ_H} for the E_{11L}^M and E_{11H}^M cutting lines [I^μ is defined in Eq. (12)]. Then, we should add the two contributions I^{μ_L} and I^{μ_H} and take the absolute value squared, i.e., $|I^{\mu_L} + I^{\mu_H}|^2$. In this way, the phase factors in I^{μ_L} and I^{μ_H} are considered and thus the interference between these two contributions is included. If we calculate the total intensity by adding the two amplitudes squared, i.e., $|I^{\mu_L}|^2 + |I^{\mu_H}|^2$, the interference effect between I^{μ_L} and I^{μ_H} is removed. In order to see how the sign of M determines the positive or negative interference effect, we also calculate the intensity by taking $|M|$ instead of M as the e-ph matrix element in Eq. (12). We discuss below the corresponding excitation profiles.

In Fig. 6(a), the resonance Raman profile is plotted for an (8,5) tube, whose energy E_{11H}^M is about 2.90 eV. The corresponding θ_N^M value for the node for $E_{11H}^M = 2.90$ eV is about 24°, which is close to 22°, the chiral angle of the (8,5) tube. Thus, due to the node effect, (8,5) tubes have a very low intensity for the E_{11}^M higher energy peak.

If $|M|$ for the higher energy peak is not small, we have three other kinds of possible RRPs which are shown in Figs. 6(b)–6(d). In the RRP for the RBM for samples with large γ, each peak has a width of about $4\gamma + E_{RBM}$. When the splitting energy $\Delta E_{11}^M < 4\gamma + E_{RBM}$, the contributions to the RRP from the lower and higher energy peaks have an overlap and a quantum interference occurs [see Fig. 6(b)]. The solid and

TABLE II. The conditions and characteristics of the four kinds of RRPs in the Stokes process for the RBM. The types $R_1 - R_4$ correspond to the cases shown in Figs. 6(a)–6(d), respectively.

	Conditions	Characteristics	Interference	Chirality
R_1	$\theta \approx 30.27 - 2.17 E_{11H}^M$	Only E_{11L}^M peak	No interference	θ large
R_2	$2\gamma + E_{\text{RBM}}/2 < \Delta E_{11}^M < 4\gamma + E_{\text{RBM}}$	Two peaks	Positive effect	θ small
R_3	$2\gamma < \Delta E_{11}^M < 2\gamma + E_{\text{RBM}}/2$	One peak	Strong positive effect	
R_4	$\Delta E_{11}^M < 2\gamma$	One weak peak	Negative effect	θ large

dashed lines in Fig. 6(b) are the RRPs that are calculated, respectively, by including and *NOT* including the interference effect. It is seen that the solid line has a larger intensity than the dashed line in the energy range between E_{11L}^M and E_{11H}^M. The reason is that the opposite sign in M for the lower and higher energy peaks makes the contributions from the two peaks add to each other in the laser energy range between E_{11L}^M and E_{11H}^M. This positive quantum interference effect enhances the intensity in this E_L range. This analysis indicates that if we use $|M|$ as the e-ph matrix element, i.e., the e-ph matrix element has the same sign for the lower and higher energy peaks, the interference effect should become a negative effect. Indeed, the long-dashed curve, which is calculated by taking $|M|$ as the e-ph matrix element, shows that the intensity in the energy range between E_{11L}^M and E_{11H}^M has been reduced by this negative effect.

Without the quantum interference effect, the two peaks in the intensity in Fig. 6(b) should be located at $E_{11L}^M + E_{\text{RBM}}/2$ and $E_{11H}^M + E_{\text{RBM}}/2$. The positive quantum interference tends to enhance the intensity in the energy range between E_{11L}^M and E_{11H}^M and thus the energy spacing between the two peaks in the intensity tends to decrease. We hereafter call this effect an attractive effect. The matrix element M is larger for the lower energy peak than for the higher energy peak [see upper and lower curves in Fig. 1(b)]. From Eq. (12) it is known that the intensity around the lower energy peak experiences less of an effect from the higher energy peak, while the intensity around the higher energy peak experiences more of an effect from the lower energy peak. Thus, the attractive effect mainly moves the higher energy peak toward the lower energy range, and moves the lower energy peak only slightly to the higher energy range [see Fig. 6(b)].

When the splitting energy ΔE_{11}^M is reduced to be $(4\gamma + E_{\text{RBM}})/2$, the two peaks in the intensity begin to merge and appear as one peak, as shown in Fig. 6(c) for the (12,6) tube. The attractive effect induced by the sign of M decreases the energy spacing needed for peak merging by $E_{\text{RBM}}/2$. Therefore, even though ΔE_{11}^M in Fig. 6(c) is as large as 0.13 eV, the two peaks can merge to become one peak. Actually, Fig. 6(c) (dashed and long-dashed curves) shows that when we do not consider the interference effect or when we take $|M|$ as the e-ph matrix element, the two peaks can be resolved.

When $\Delta E_{11}^M < 2\gamma$, the two peaks have a dominant overlap region. The interference effect then becomes a negative interference effect, which tends to suppress the peak intensity, as indicated by Fig. 6(d). This negative effect can be understood from Eq. (12). The Raman intensity has contributions from both the states around E_{11L}^M and around E_{11H}^M. If the E_{11L}^M and E_{11H}^M peaks in the JDOS are very close in energy, the denominator in Eq. (12) is approximately the same for the two contributions from E_{11L}^M and E_{11H}^M. However, M has an opposite sign for E_{11L}^M and E_{11H}^M. Thus, the two contributions partially cancel each other and the intensity is suppressed. If we take $|M|$ as the e-ph matrix element, the two contributions are added together and the intensity is enhanced as indicated by the long-dashed curve. The earlier discussions for the four RRPs for the RBM are summarized in Table II.

As we have pointed out, without the attractive effect the two peaks in Fig. 6 should be at $E_{11L}^M + (E_{\text{RBM}}/2)$ and $E_{11H}^M + (E_{\text{RBM}}/2)$ for the Stokes process. The attractive effect tends to reduce the energy spacing between the two peaks by $E_{\text{RBM}}/2$ and this reduction mainly comes from the change of the higher energy peak position. Thus, after including the quantum interference effect, the two peaks are at $E_{11L}^M + E_{\text{RBM}}/2$ and E_{11H}^M, respectively, for the Stokes process. Therefore, when we try to obtain the E_{iiL}^M and E_{iiH}^M energies from the RBM peak positions for metallic nanotubes, there is a correction factor of $E_{\text{RBM}}/2$ for the lower energy peak, while there is no correction factor for the higher energy peak, which downshifts by $E_{\text{RBM}}/2$. The accuracy for the E_{iiL}^M and the E_{iiH}^M values obtained by this method is better than 10 meV.

The anti-Stokes process has a similar attractive effect as the Stokes process. Thus, the two crossing points with lower and higher energies, for the Stokes and the normalized anti-Stokes intensities are at E_{iiL}^M and $E_{iiH}^M - (E_{\text{RBM}}/2)$, respectively. This means that when we try to use the anti-Stokes to Stokes intensity ratio to determine the E_{iiL}^M and E_{iiH}^M vHSs of metallic nanotubes, there is no correction factor for the crossing point in the lower energy range, while there is a correction factor of $E_{\text{RBM}}/2$ for the crossing point position in the higher energy range.

In Fig. 6, the tubes (13,4), (12,6), and (11,8) have similar diameters but different chiral angles. Figures 6(b)–6(d) indicate that the intensity decreases with increasing chiral angle, which follows from the chiral angle dependence of the e-ph matrix element (see Sec. III) and is consistent with experimental observation.[15,16]

2. Small γ case

For the small γ case, we have two common kinds of RRPs for the Stokes process and they are shown in Fig. 7, where the RRPs are calculated by taking $\gamma = 0.006$ eV. Figure 7(a) is plotted for the (11,8) tube, which has a $E_{11H}^M = 1.96$ eV and a chiral angle $\theta \approx 25°$. From Eq. (10), θ_N for $E_{11H}^M = 1.96$ eV is about 26°, which is close to 25°, the chiral angle of the (11,8) tube. Correspondingly, the higher energy
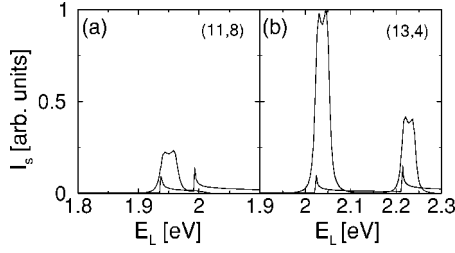
FIG. 7. Illustration of the two kinds of RRPs in the Stokes process for the RBM in metallic nanotubes (a) (11,8) and (b) (13,4) calculated with $\gamma=0.006$ eV. The joint density of states are given to show the vHS peak positions.
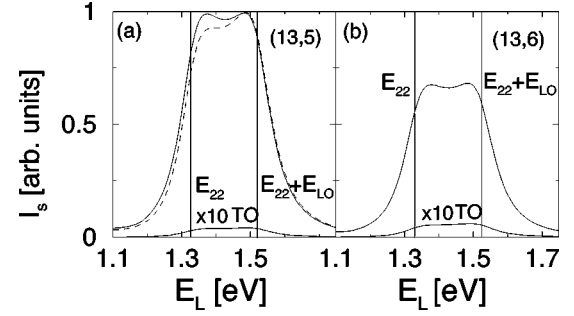

FIG. 8. Raman intensity for the Stokes process for the G band A symmetry mode vs excitation energy E_L for (a) an SI (13,5) and (b) an SII (13,6) semiconducting tube where $\gamma=0.06$ eV is used in the calculations. The dashed line in (a) is the calculated profile by eliminating the interference effect between the E_{11}^S and E_{22}^S bands.

peak has a very low intensity due to the node effect. Figure 7(b) is plotted for a (13,4) tube, which represents another kind of RRP. Figure 7(b) shows two peaks for the lower and higher energy vHSs, and each peak is further split into incident and scattered peaks. For the small γ case, in the RRP for the RBM, the intensity width including both the incident and scattered peaks for one vHS energy peak is about $4\gamma + E_{RBM}$. In order to have a quantum interference effect, the splitting energy ΔE_{11}^M should be smaller than $4\gamma + E_{RBM} \approx 0.045$ eV, which means $d_t > 1.4$ nm and $\theta > 22°$. From Fig. 1(b), we know that M for the higher energy peak [lower curves in Fig. 1(b)] is small when $\theta > 22°$. It follows that even though there is an interference effect for nanotubes with $d_t > 1.4$ nm and $\theta > 22°$, the interference effect should be weak due to the small M for the higher energy peak. Thus, we can neglect the interference effect in the RBM intensity for the small γ case. Therefore, for this case, we do not need a correction factor when we try to get E_{iiL}^M and E_{iiH}^M by analyzing the RBM intensity. Moreover, due to the small γ value and the lack of a quantum interference effect, this kind of a sample is a good candidate for observation of the RBM intensity for the higher energy E_{iiH}^M peak.

V. G BAND A SYMMETRY MODE RESONANCE RAMAN EXCITATION PROFILES

The G band Raman intensity for the A symmetry TO and LO phonon modes is calculated by using Eq. (11). The G band phonon modes have much larger energies than for the RBM and thus, even for the large γ case, the incident and scattered resonance peaks should be resolved. Experimentally, by varying the laser energy E_L, the G band intensity is observed most of the time, which is different from the RBM feature which appears and disappears quickly as E_L is varied. This is also related to the large E_{ph} for the G band phonon modes, considering the broadening factor γ.

A. Semiconducting nanotubes

Figure 8 shows the RRP for the Stokes process for the G band A symmetry mode for the E_{22}^S transition for (a) an SI (13,5) tube and (b) an SII (13,6) tube. The RRP is calculated by taking $\gamma=0.06$ eV. Figure 8 shows that the LO mode has a larger intensity than the TO mode. Furthermore, for the LO mode, the (13,5) tube has a larger intensity than the (13,6)

tube, while for the TO mode the (13,5) tube has a slightly smaller intensity than the (13,6) tube, which follows from the tube type dependence of the e-ph matrix elements of the G band A symmetry mode shown in Fig. 2. In comparison to the intensity for the RBM (see Fig. 3), the intensity for the G band has a weaker tube type dependence. In addition, we note that the two peaks in the intensity in Fig. 8 have been shifted in an attractive way from E_{22}^S and $E_{22}^S + E_{LO}$. In comparison with the RBM, the shift energy here is larger. The reason is that due to the large γ and phonon energy, we have a broadening intensity width for the E_{22}^S transition, where the two peaks for the incident and scattered resonance have a large overlap in their contributions to the intensity. Thus, more states in the E_{11}^S and E_{22}^S bands make a contribution to the intensity in comparison to the RBM and therefore the shift energy becomes larger. From the solid and dashed curves in Fig. 8 for the LO mode, we see that the interference effect between the E_{11}^S and E_{22}^S bands tends to enhance the ratio of the incident resonance peak intensity to the scattered resonance peak intensity for the LO mode. Thus, unlike the case for the RBM, to obtain the correct RRP shape for the LO mode, the e-ph matrix element M should be considered, since M has an opposite sign for the E_{11}^S and E_{22}^S cutting lines.

The corresponding RRPs obtained by taking $\gamma=0.006$ eV are plotted in Fig. 9. For this case the intensity peaks are very close in energy to E_{22}^S and $E_{22}^S + E_{LO}$, which suggests that we can also determine the E_{ii} energies properly from the intensity peak positions of the LO mode for freely suspended nanotubes.

B. Metallic nanotubes

Due to the presence of free electrons, G band scattering from metallic nanotubes shows asymmetrically broadened Breit-Wigner-Fano line shapes around the TO mode frequency range,[37] which will not be discussed here. Thus, for metallic nanotubes we focus on the LO mode, which has a frequency of about 1590 cm^{-1}. As we have pointed out, if we substitute SI and SII in Fig. 2(a) by E_{11L}^M and E_{11H}^M, respectively, we will get a plot similar to the plot for the A symmetry LO mode for metallic nanotubes. For the LO mode,
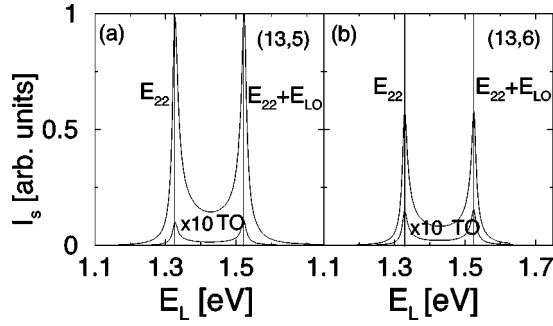
FIG. 9. Raman intensity for the Stokes process for the *G* band *A* symmetry mode vs excitation energy E_L for (a) an SI (13,5) tube and (b) an SII (13,6) tube where $\gamma = 0.006$ eV is used in the calculations.

the e-ph matrix element *M* has an opposite sign outside and inside the 2D BZ. Thus, the sign of *M* also plays an important role in determining the RRP for the LO mode in metallic nanotubes. For the LO mode, the interference effect becomes more complicated, since there are both incident and scattered resonance peaks for each vHS feature and there is also a trigonal warping effect, which splits one vHS peak E_{ii}^M into two peaks E_{iiL}^M and E_{iiH}^M.

For the large γ case, the four kinds of RRPs are shown in Figs. 10(a)–10(d), where γ is taken as 0.06 eV. In the RRP for the LO mode, the intensity width, including both the incident and scattered peaks, for one vHS feature is about $4\gamma + E_{\mathrm{LO}}$. If $\Delta E_{11}^M > 4\gamma + E_{\mathrm{LO}}$, the interference effect between E_{11L}^M and E_{11H}^M is weak and four peaks should be seen. Figure 10(a) shows this case for a (9,0) SWNT, where four peaks can be resolved.

When $\Delta E_{11}^M < 4\gamma + E_{\mathrm{LO}}$, the positive interference effect induces an attractive effect, which tends to enhance the intensities of the two middle peaks [see Fig. 10(b) for a (9,3) SWNT]. For the case of $\Delta E_{11}^M < 2\gamma + E_{\mathrm{LO}}$, the two peaks in the middle region are merged into one peak due to the attractive effect between the E_{11L}^M scattered and E_{11H}^M incident peaks. We show this case in Fig. 10(c) for the (12,3) SWNT, where we can see a central peak with high intensity and two humps on the left and right sides of this peak.

When ΔE_{11}^M is further reduced to be $\Delta E_{11}^M < 2\gamma$, the two features, including all four peaks, around E_{11L}^M and E_{11H}^M try to merge into one peak, since the broadening factor γ is large compared to other energies [see dashed curves in Fig. 10(d) for the (11,8) tube]. However, in this case the interference effect turns out to be a negative interference effect, which
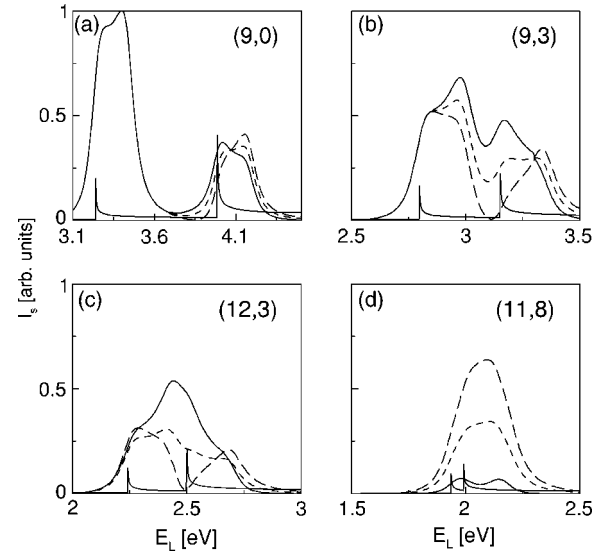

FIG. 10. Illustration of the four kinds of RRPs for the Stokes process for the LO mode in metallic nanotubes (a) (9,0), (b) (9,3), (c) (12,3), and (d) (11,8). The profiles calculated by eliminating the interference effect and the profiles calculated by taking |*M*| as the electron-phonon matrix element are also shown by dashed and long-dashed curves. The joint density of states are given to show the vHS peak splitting energy. The broadening factor $\gamma = 0.06$ eV is used in the calculations.

suppresses the peak intensities and it further separates the peak positions. Thus, from the solid curve of Fig. 10(d), we see two distinct peaks but with suppressed intensity.

It is worth noting that, for the large γ case, types (a) and (b) in Fig. 10 should be observable only when $\Delta E_{11}^M > 2\gamma + E_{\mathrm{LO}} \approx 0.22$ eV, which means that d_t should be smaller than 1nm. For nanotubes with $d_t > 1$ nm, we can get only two kinds of RRPs, i.e., cases (c) and (d) in Fig. 10. The properties of the four kinds of LO RRPs are listed in Table III.

For the large γ case, in order to observe the RRP type where four peaks are resolved, we have to choose small diameter nanotubes. However, this RRP type becomes a common type for the small γ case. By taking $\gamma = 0.006$ eV, we find two types of RRPs, which are shown in Fig. 11 and here Fig. 11(a) represents a common type. Figure 11(b) shows another type of RRP, where the middle two peaks are merged into one peak. This type can appear only when the splitting energy $\Delta E_{11}^M \approx E_{\mathrm{LO}}$.

TABLE III. The conditions and characteristics of the four kinds of RRPs associated with the *A* symmetry LO mode for metallic SWNTs. The types L_1-L_4 correspond to the cases shown in Figs. 6(a)–6(d), respectively.

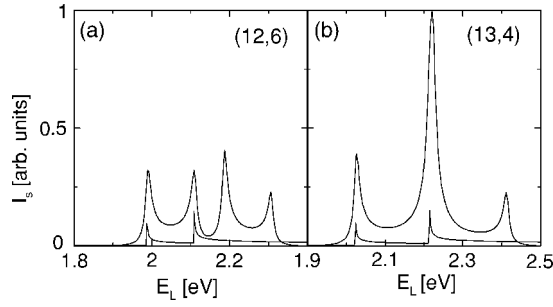|	Conditions	Characteristics	Interference	Chirality
L_1	$\Delta E_{11}^M < 4\gamma + E_{\mathrm{LO}}$	Four peaks	Negligible	d_t small
L_2	$2\gamma + E_{\mathrm{LO}} < \Delta E_{11}^M < 4\gamma + E_{\mathrm{LO}}$	Enhanced middle peaks	Positive effect	d_t small
L_3	$2\gamma < \Delta E_{11}^M < 2\gamma + E_{\mathrm{LO}}$	One high peak, two humps	Strong positive effect	
L_4	$\Delta E_{11}^M < 2\gamma$	Two peaks	Negative effect	θ small

FIG. 11. Illustration of the two kinds of RRPs calculated for the Stokes process for the LO mode in metallic nanotubes for the (a) (12,6) and (b) (13,4) SWNTs and using $\gamma = 0.006$ eV. The joint density of states curves are plotted to show the vHS peak position.

VI. GUIDANCE FOR EXPERIMENTALISTS

For the samples with small γ, the RBM intensity peaks are clear and one can easily find the E_{ii} values. For the samples with large γ (as defined earlier), the incident and scattered peaks merge together. A simple and easy way to find a good estimate for the E_{ii} values, rather than by making a detailed fit, is just to consider the peak position minus the correction factor $E_{RBM}/2$. For metallic nanotubes, the quantum interference effect introduces an additional energy shift for the intensity peak positions and a proper correction factor is also found and listed in Table IV. By using the correction factors in Table IV, the E_{ii} values thus obtained have an accuracy up to 10 meV.

By taking $\gamma = 0.06$ eV, we calculate the RBM intensity in the Stokes process for the E_{22}^S transition for semiconducting tubes (I_2^S) and the E_{11L}^M transition for metallic tubes (I_1^M) with diameters in the range of 0.6–1.6 nm. For SI tubes and SII tubes, a functional form of $I_2^S(d_t, \theta)$ can be obtained by fitting the calculated $I_2^S(n,m)$ with

$$\frac{I_2^S(d_t, \theta)}{C} = \frac{A_2^S}{d_t} + \frac{B_2^S}{d_t^2} + \left(\frac{C_2^S}{d_t} + \frac{D_2^S}{d_t^2} \right) \cos(3\theta) \qquad (14)$$

For SII tubes, there are nodes for the e-ph matrix element in the high chiral angle range. Thus, we have two sets of fitting parameters for $\theta < 25°$ and $\theta \geq 25°$, respectively. For metallic nanotubes, a functional form for $I_1^M(d_t, \theta)$ is obtained by fitting the calculated $I_1^M(n,m)$ with

$$\frac{I_1^M(d_t, \theta)}{C} = \frac{A_1^M}{d_t} + \frac{B_1^M}{d_t^2} + \left(\frac{C_1^M}{d_t} + \frac{D_1^M}{d_t^2} \right) \cos(3\theta) \qquad (15)$$

Armchair tubes are special metallic nanotubes since they have two vHSs around the same K point for the E_{11}^M transi-

TABLE IV. The peak positions in the RBM intensity and the crossing point positions of the Stokes and normalized anti-Stokes RBM intensities. M and S represent metallic and semiconducting nanotubes, respectively.

Type	Peak position	S/AS crossing point position
S	$E_{ii}^S + (E_{RBM}/2)$	E_{ii}^S
M	$E_{iiL}^M + (E_{RBM}/2), E_{iiH}^M$	$E_{iiL}, E_{iiH}^M - (E_{RBM}/2)$

TABLE V. The fitting parameters for the intensity $I_2^S(n,m)$ for semiconducting nanotubes and $I_1^M(n,m)$ for metallic nanotubes.

Type	A (nm)	B (nm²)	C (nm)	D (nm²)
SI	−0.03187	−0.04106	0.07297	0.4163
SII ($\theta < 25°$)	0.09683	−0.2997	0.03431	0.4300
SII ($\theta \geq 25°$)	−0.0005478	0.03230	−0.26691	0.01084
M	−0.05525	−0.06549	0.05871	0.7578
Armchair	−0.2634	0.4302	0	0

tion. Thus, they have a different set of fitting parameters. The common constant C in Eqs. (14) and (15) is a tube-independent constant. The fitting parameters in Eqs. (14) and (15) are listed in Table V.

Figures 1(a) and 1(b) tell us that due to the nodes of the e-ph matrix element for the vHSs inside the 2D BZ, the SII and metallic tubes around the nodes have a very weak RBM intensity for the E_{22}^S and E_{11H}^M transitions, respectively. Figure 6 tells us that for the SDS wrapped metallic nanotubes, the two peaks in the RRP are merged into one peak when the energy spacing ΔE_{11}^M between the two vHS peaks in the JDOS due to the trigonal warping effect is smaller than $2\gamma + E_{RBM}/2 \approx 0.13$ eV. By summarizing these results, we can classify SII and metallic tubes into three kinds according to their RBM RRP characteristics for the E_{22}^S and E_{11}^M transitions, respectively. The result is shown in Fig. 12, where two curves are drawn, i.e., curves 1 and 2. Above curve 1, the SII tubes have a large intensity and metallic tubes show a two-peak feature. Below curve 2 is a node region, where the SII tubes have a very weak intensity and metallic tubes have a very weak intensity for the higher energy peak, since the vHSs for these tubes are close to nodes. The region between curves 1 and 2 is a special region, where the SDS wrapped metallic nanotubes only show a one peak RBM feature due to the strong interference effect. Freely suspended SWNTs or SWNTs on a Si substrate can, however, show two peaks. Thus, this is a region sensitive to the broadening factor γ of the samples. SII tubes in this region also are predicted to show a large intensity. Figure 12 thus can be used to identify metallic nanotubes, which may show a two peak feature in RBM intensity measurements.

VII. SUMMARY

In summary, we have used our calculated e-ph matrix element to interpret first-order Raman processes under various experimental conditions. The theory of the e-ph matrix element can well explain the observed chirality-dependent properties of the RBM and G band A symmetry mode resonance Raman intensities. For semiconducting nanotubes, the RRPs are calculated for both SI and SII semiconducting tubes in the large and small γ (line broadening) regimes. We find that the e-ph matrix has a negligible effect on the RRP shape for the RBM, while the e-ph matrix must be considered to obtain correct RRP shapes for the LO mode, since the quantum interference effect between the states for E_{11}^S and E_{22}^S bands for the LO mode cannot be neglected.
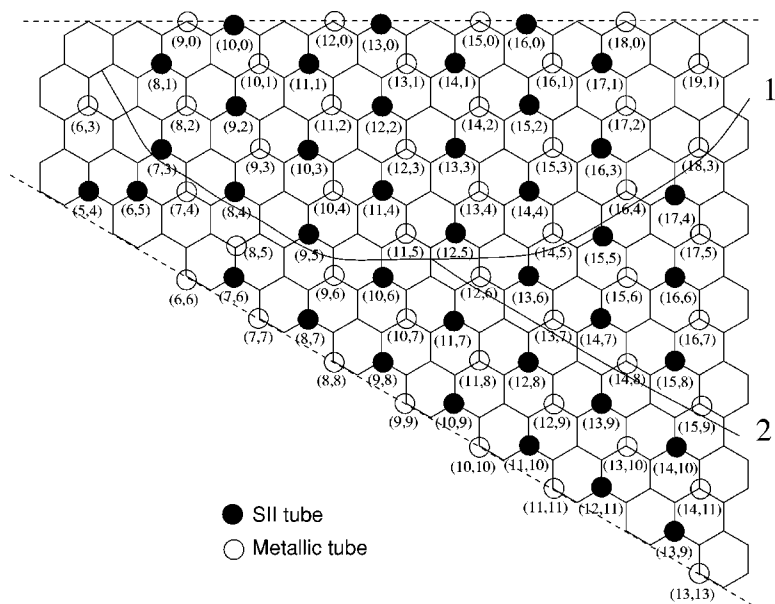
FIG. 12. Classification of the SII and metallic nanotubes according to their characteristics in the RBM Raman spectra. Curves 1 and 2 delineate three regions (see text).

Motivated by the observation of the opposite sign in both the RBM and LO mode matrix elements inside and outside the 2D BZ, we have studied the interference effect in the Raman spectra for metallic nanotubes due to the trigonal warping effect. The calculated results can explain the experimentally observed missing RBM Raman signals for the higher energy vHS peaks for SDS wrapped metallic nanotubes. Different types of RRPs for metallic nanotubes in the large and small γ regimes are found.

We calculate the RBM intensity for the E_{22}^S transition for semiconducting nanotubes and for the E_{11L}^M transition for metallic nanotubes. The functions describing the diameter and chiral angle dependence of the RBM intensity are found.

In summarizing the main results in the paper, we find three different regimes for (n,m) indices according to their RBM spectra characteristics. From these three regimes one can easily predict which (n,m) tubes are expected to have strong or weak RBM intensity and which (n,m) metallic tubes may show a two peak feature in the RBM intensity measurement.

We did not consider exciton effects in this paper. Exciton effects are important for small diameter semiconducting nanotubes. The influence of exciton effects on the Raman intensities studied here will be addressed in a future work.

ACKNOWLEDGMENTS

[1] A. M. Rao, E. Richter, S. Bandow, B. Chase, P. C. Eklund, K. A. Williams, S. Fang, K. R. Subbaswamy, M. Menon, A. Thess, R. E. Smalley, G. Dresselhaus, and M. S. Dresselhaus, Science **275**, 187 (1997).

[2] M. S. Dresselhaus, G. Dresselhaus, R. Saito, and A. Jorio, Phys. Rep. **409**, 47 (2005).

[3] S. M. Bachilo, M. S. Strano, C. Kittrell, R. H. Hauge, R. E. Smalley, and R. B. Weisman, Science **298**, 2361 (2002).

[4] M. S. Dresselhaus, G. Dresselhaus, and P. C. Eklund, *Science of Fullerenes and Carbon Nanotubes* (Academic, New York, 1996).

[5] S. Bandow, S. Asaka, Y. Saito, A. M. Rao, L. Grigorian, E. Richter, and P. C. Eklund, Phys. Rev. Lett. **80**, 3779 (1998).

[6] M. Milnera, J. Kürti, M. Hulman, and H. Kuzmany, Phys. Rev. Lett. **84**, 1324 (2000).

[7] A. Jorio, R. Saito, J. H. Hafner, C. M. Lieber, M. Hunter, T. McClure, G. Dresselhaus, and M. S. Dresselhaus, Phys. Rev. Lett. **86**, 1118 (2001).

[8] C. Kramberger, R. Pfeiffer, H. Kuzmany, V. Zólyomi, and J. Kürti, Phys. Rev. B **68**, 235404 (2003).

[9] R. R. Bacsa, A. Peigney, C. Laurent, P. Puech, and W. S. Bacsa, Phys. Rev. B **65**, 161404(R) (2002).

[10] R. Saito, G. Dresselhaus, and M. S. Dresselhaus, *Physical Properties of Carbon Nanotubes* (Imperial College Press, London, 1998).

[11] D. Kahn and J. P. Lu, Phys. Rev. B **60**, 6535 (1999).

[12] A. Kasuya, Y. Sasaki, Y. Saito, K. Tohji, and Y. Nishina, Phys. Rev. Lett. **78**, 4434 (1997).

[13] A. Kasuya, M. Sugano, T. Maeda, Y. Saito, K. Tohji, H. Takahashi, Y. Sasaki, M. Fukushima, Y. Nishina, and C. Horie, Phys. Rev. B **57**, 4999 (1998).

[14] A. Jorio, G. Dresselhaus, M. S. Dresselhaus, M. Souza, M. S. S. Dantas, M. A. Pimenta, A. M. Rao, R. Saito, C. Liu, and H. M. Cheng, Phys. Rev. Lett. **85**, 2617 (2000).

[15] R. Saito, A. Jorio, J. H. Hafner, C. M. Lieber, M. Hunter, T. McClure, G. Dresselhaus, and M. S. Dresselhaus, Phys. Rev. B

64, 085312 (2001).

[16] Z. Yu and L. E. Brus, J. Phys. Chem. B **105**, 1123 (2001).

[17] M. Machón, S. Reich, H. Telg, J. Maultzsch, P. Ordejón, and C. Thomsen, Phys. Rev. B **71**, 035416 (2005).

[18] V. N. Popov, L. Henrard, and P. Lambin, Nano Lett. **4**, 1795 (2004).

[19] J. Jiang, R. Saito, A. Grüneis, G. Dresselhaus, and M. S. Dresselhaus, Chem. Phys. Lett. **392**, 383 (2004).

[20] J. Jiang, R. Saito, A. Grüneis, S. G. Chou, Ge. G. Samsonidze, A. Jorio, G. Dresselhaus, and M. S. Dresselhaus, Phys. Rev. B **71**, 045417 (2005).

[21] A. Grüneis. PhD thesis, Tohoku University, Sendai, Japan, September 2004.

[22] K. Seibert, G. C. Cho, W. Kütt, H. Kurz, D. H. Reitze, J. I. Dadap, H. Ahn, M. C. Downer, and A. M. Malvezzi, Phys. Rev. B **42**, 2842 (1990).

[23] T. Hertel and G. Moos, Chem. Phys. Lett. **320**, 359 (2000).

[24] T. Hertel and G. Moos, Phys. Rev. Lett. **84**, 5002 (2000).

[25] J. S. Lauret, C. Voisin, G. Cassabois, C. Delalande, Ph. Roussignol, O. Jost, and L. Capes, Phys. Rev. Lett. **90**, 057404 (2003).

[26] Y.-Z. Ma, J. Stenger, J. Zimmermann, S. M. Bachilo, R. E. Smalley, R. B. Weisman, and G. R. Fleming, J. Chem. Phys. **120**, 3368 (2004).

[27] H. Hippler, A.-N. Unterreiner, J.-P. Yang, S. Lebedkin, and M. M. Kappes, Phys. Chem. Chem. Phys. **6**, 2387 (2004).

[28] S. G. Chou, H. B. Ribeiro, E. Barros, A. P. Santos, D. Nezich, Ge. G. Samsonidze, C. Fantini, M. A. Pimenta, A. Jorio, F. Plentz Filho, M. S. Dresselhaus, G. Dresselhaus, R. Saito, M. Zheng, G. B. Onoa, E. D. Semke, A. K. Swan, M. S. Ünlü, and B. B. Goldberg, Chem. Phys. Lett. **397**, 296 (2004).

[29] S. G. Chou, F. Plentz, J. Jiang, R. Saito, D. Nezich, H. B. Ribeiro, A. Jorio, M. A. Pimenta, Ge. G. Samsonidze, A. P. Santos, M. Zheng, G. B. Onoa, E. D. Semke, G. Dresselhaus, and M. S. Dresselhaus, Phys. Rev. Lett. **94**, 127402 (2005).

[30] E. Richter and K. R. Subbaswamy, Phys. Rev. Lett. **79**, 2738 (1997).

[31] H. Ajiki and T. Ando, Physica B **201**, 349 (1994).

[32] A. Jorio, C. Fantini, M. A. Pimenta, R. B. Capaz, Ge. G. Samsonidze, G. Dresselhaus, M. S. Dresselhaus, J. Jiang, N. Kobayashi, A. Grüneis, R. Saito, Phys. Rev. B **71**, 075401 (2005).

[33] C. Fantini, A. Jorio, M. Souza, M. S. Strano, M. S. Dresselhaus, and M. A. Pimenta, Phys. Rev. Lett. **93**, 147406 (2004).

[34] M. J. O'Connell, S. M. Bachilo, X. B. Huffman, V. C. Moore, M. S. Strano, E. H. Haroz, K. L. Rialon, P. J. Boul, W. H. Noon, C. Kittrell, J. Ma, R. H. Hauge, R. B. Weisman, and R. E. Smalley, Science **297**, 593 (2002).

[35] A. G. Souza Filho, S. G. Chou, Ge. G. Samsonidze, G. Dresselhaus, M. S. Dresselhaus, Lei An, J. Liu, Anna K. Swan, M. S. Ünlü, B. B. Goldberg, A. Jorio, A. Grüneis, and R. Saito, Phys. Rev. B **69**, 115428 (2004).

[36] A. Jorio, A. G. Souza Filho, G. Dresselhaus, M. S. Dresselhaus, R. Saito, J. H. Hafner, C. M. Lieber, F. M. Matinaga, M. S. S. Dantas, and M. A. Pimenta, Phys. Rev. B **63**, 245416 (2001).

[37] H. Kataura, Y. Kumazawa, Y. Maniwa, I. Umezu, S. Suzuki, Y. Ohtsuka, and Y. Achiba, Synth. Met. **103**, 2555 (1999).

[38] R. Saito, G. Dresselhaus, and M. S. Dresselhaus, Phys. Rev. B **61**, 2981 (2000).

[39] C. D. Spataru, S. Ismail-Beigi, L. X. Benedict, and S. G. Louie, Phys. Rev. Lett. **92**, 077402 (2004).

[40] V. N. Popov, New J. Phys. **6**, 17 (2004).

[41] J. Jiang, R. Saito, A. Grüneis, G. Dresselhasu, and M. S. Dresselhasu, Carbon **42**, 3169 (2004).

[42] A. Grüneis, R. Saito, Ge. G. Samsonidze, T. Kimura, M. A. Pimenta, A. Jorio, A. G. Souza Filho, G. Dresselhaus, and M. S. Dresselhaus, Phys. Rev. B **67**, 165402 (2003).

[43] Ge. G. Samsonidze, R. Saito, N. Kobayashi, A. Grüneis, J. Jiang, A. Jorio, S. G. Chou, G. Dresselhaus, and M. S. Dresselhaus, Appl. Phys. Lett. **85**, 5703 (2004).

[44] H. Kataura, Y. Kumazawa, N. Kojima, Y. Maniwa, I. Umezu, S. Masubuchi, S. Kazama, X. Zhao, Y. Ando, Y. Ohtsuka, S. Suzuki, and Y. Achiba, in *Proceedings of the International Winter School on Electronic Properties of Novel Materials (IWEPNM'99)*, edited by H. Kuzmany, M. Mehring, and J. Fink, AIP Conf. Proc. No. 486 (American Institute of Physics, Woodbury, NY, 1999), pp. 328.

[45] A. Jorio, A. G. Souza Filho, G. Dresselhaus, M. S. Dresselhaus, A. K. Swan, M. S. Ünlü, B. Goldberg, M. A. Pimenta, J. H. Hafner, C. M. Lieber, and R. Saito, Phys. Rev. B **65**, 155412 (2002).

[46] R. M. Martin and L. M. Falicov, in *Light-Scattering in Solids*, edited by M. Cardona (Springer-Verlag, Berlin, 1975), p. 80.